processes

MDPI

Article

Advanced Insights into Methane Hydrate Production: Influence of Pressure, Saturation, and Permeability Dynamics

Yunjian Zhou [1,2], Yufa He [1,2], Yu Chen [1] and Shihui Sun [3,*]

[1] CNOOC Research Institute Ltd., Beijing 100028, China
[2] Huairou Laboratory, Beijing 100028, China
[3] Sanya Offshore Oil & Gas Research Institute, Northeast Petroleum University, Sanya 572025, China
* Correspondence: sshsmile@163.com

Abstract: The decomposition of hydrate during hydrate mining can reduce the strength of the formation and induce engineering geological disasters. Clarifying the decomposition characteristics of geological hydrate during hydrate mining is of great significance for preventing marine geological disasters. This study comprehensively examines the effects of various extraction conditions, including production pressure, hydrate saturation, and permeability, on methane hydrate decomposition during depressurization-based extraction. Key findings show that reduced production pressure significantly increases gas and water production rates due to an enhanced pressure differential, albeit at the cost of potential geomechanical instability. Variations in hydrate saturation reveal that lower-saturation reservoirs initially exhibit higher production due to faster pressure propagation and greater porosity, whereas high-saturation layers may sustain production in the later stages. Permeability changes impact pressure diffusion and heat transfer within the formation; higher permeability leads to faster initial production but causes rapid energy depletion, requiring supplementary energy inputs to maintain production. These findings provide essential insights for optimizing methane hydrate extraction, ensuring high productivity while mitigating formation stability risks.

Keywords: methane hydrate; depressurization; production pressure; permeability; gas production

check for updates

Academic Editor: Qingbang Meng

Received: 18 November 2024
Revised: 27 December 2024
Accepted: 29 December 2024
Published: 1 January 2025

Citation: Zhou, Y.; He, Y.; Chen, Y.; Sun, S. Advanced Insights into Methane Hydrate Production: Influence of Pressure, Saturation, and Permeability Dynamics. *Processes* **2025**, *13*, 80. https://doi.org/10.3390/pr13010080

Copyright: © 2025 by the authors. Licensee MDPI, Basel, Switzerland. This article is an open access article distributed under the terms and conditions of the Creative Commons Attribution (CC BY) license (https://creativecommons.org/licenses/by/4.0/).

1. Introduction

Deep-water oil and gas resources are considered a vital frontier in the field of petroleum exploration, drawing substantial investment from developed nations like the United States and the United Kingdom [1,2]. Among these resources, gas hydrates, a type of unconventional hydrocarbon found beneath deep-sea sediment layers, are of particular interest. Global reserves of gas hydrates are estimated at around 2×10^{16} cubic meters, with organic carbon content representing approximately 53.3% of the total global organic carbon [3–5]. Notably, the total carbon stored in gas hydrates is estimated to be nearly double that contained in all existing fossil fuels (including oil, natural gas, and coal) on Earth. Gas hydrates are widely distributed, covering about 27% of terrestrial areas (mainly in permafrost regions) and up to 90% of marine environments [6]. On land, gas hydrates are generally found at depths between 200 and 2000 m, whereas in subsea sediments, they are typically located at depths of 500 to 800 m [7]. Moreover, gas hydrates exhibit significant extraction potential due to their lower carbon emissions and higher energy density, positioning them as a valuable resource for mitigating climate change, promoting clean energy development, and reducing dependence on conventional fossil fuels.

During extraction, changes in temperature and pressure cause gas hydrates to dissociate, releasing methane gas and water. This dissociation process can lead to reduced strength in hydrate-bearing formations, altering the mechanical properties of the strata and increasing the risk of engineering and geological hazards [8,9]. The impact of gas hydrate dissociation on formation strength is a complex, multi-faceted process, particularly pronounced in deep-sea sediments and permafrost zones. Gas hydrates typically exist in crystalline form within sediment pores, forming a stable, solid structure under low-temperature, high-pressure conditions [10,11]. These solid gas hydrates not only occupy pore spaces, but also provide structural support. However, as temperatures rise or pressures fall, the hydrates dissociate, releasing methane gas and water, which increases pore pressure [12,13]. The rise in pore pressure reduces the friction between sediment particles, thereby lowering the shear strength of the formation. This process makes the formation more susceptible to sliding and collapse [14,15].

Of particular importance, gas released from dissociated hydrates occupies pore spaces, causing the sediment particle structure to become loose. As the supportive hydrate crystals disappear, points of contact between particles decrease, resulting in reduced cohesion and stability of the sediment [16,17]. Gas pockets may even form within the sediment, further weakening consolidation and potentially creating gas bubbles that destabilize the structure, especially in deeper layers. Once the formation strength is compromised, localized subsidence or compression may occur, triggering extensive deformation in the formation [18].

In sloping seabed regions, particularly deep-sea slope areas, gas hydrate dissociation significantly increases the risk of landslides or sediment slippage. The combination of elevated pore pressure and reduced formation strength decreases the sediment's shear resistance, making it more prone to sliding under external forces, such as earthquakes, wave action, or human intervention [19,20]. For oil and gas exploration and drilling operations, these changes in formation strength may result in wellbore instability. If the drilling wellbore penetrates a hydrate-bearing layer, gas hydrate dissociation can destabilize the well walls and even lead to blowouts, posing risks to equipment and the environment. Therefore, hydrate dissociation in deep-sea and permafrost regions impacts formation strength and presents substantial challenges to regional environments, subsea ecosystems, and engineering infrastructure.

Considering the factors of economic viability, feasibility, safety, and environmental protection, depressurization is currently the dominant method for gas hydrate extraction. Prolonged depressurization causes extensive hydrate dissociation and lowers formation pressure, increasing the risk of wellbore instability. Field tests of marine gas hydrates in countries like Russia, the United States, Canada, and Japan have observed instances of wellbore collapse and instability [21]. This study conducts a series of numerical simulations on hydrate dissociation during depressurization extraction to provide insights for enhancing the safety of hydrate extraction. According to the previous research by domestic and international scholars, the initial formation strength in hydrate-bearing strata is three-to-nine-times higher than that after hydrate dissociation [22].

The dissociation of hydrates reduces their supporting role within the formation and alters in situ stress, disrupting surrounding stress fields, temperature fields, and seepage fields, which in turn decreases wellbore strength and increases formation instability risks. Additionally, hydrate dissociation increases the water content in the formation, weakening the cementation between hydrate particles, and further destabilizes the wellbore. Gas released from dissociated hydrates affects the density and rheology of drilling fluids, compounding the adverse impact on wellbore temperature. Therefore, studying the effects

of various influencing factors on hydrate dissociation is crucial for predicting formation stability and guiding engineering planning.

In summary, against the backdrop of geological parameters in the Shenhu Sea area, this study focuses on examining the characteristics of hydrate decomposition under varying wellbore sizes, perforation lengths, extraction pressures, hydrate saturations, and permeabilities to provide data support for hydrate wellbore stability research. Additionally, the effects of these factors on reservoir and production parameters were analyzed to assess their impact on gas production from natural gas hydrates. These findings contribute to the selection of extraction areas and the design of extraction parameters for hydrate exploitation in the Shenhu area of the South China Sea.

2. Materials and Methods

2.1. Research Background and Basic Assumptions

This study uses the gas hydrate reservoir in the clayey silt layers of the Shenhu area in the South China Sea as a prototype. In 2015, during the third gas hydrate drilling expedition (GMGS3) by the China Geological Survey, high-saturation gas hydrates were discovered between 135 m and 157 m below the seafloor at the GMGS3-W19 site [23]. The GMGS3-W19 site is located on the northern slope of the Shenhu area in the South China Sea, as shown in Figure 1. Based on the well logs from GMGS3-W19, the gas saturation at this site reaches up to 45%, with a porosity of 48% and a hydrate reservoir thickness of approximately 35.9 m [24]. The formation's lithology has been preliminarily identified as clayey silt with permeability measured in millidarcies (mD).

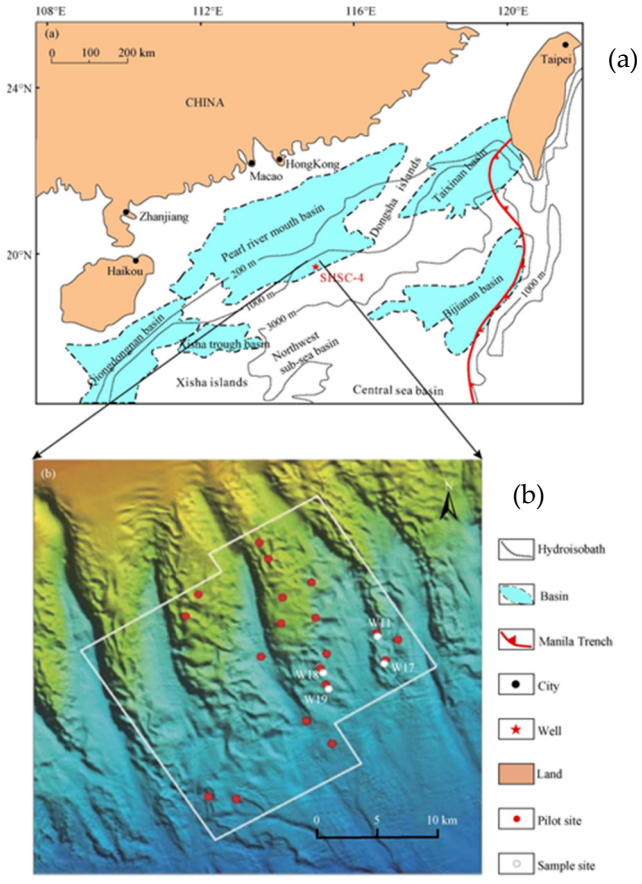


Figure 1. Distribution of site GMGS3-W19 in the Shenhu area, Northern South China Sea (cited from [23]). (**a**) topographic map; (**b**) site map.

Wellbore stability during gas hydrate extraction is governed by a complex process involving heat transfer, seepage, and mechanical coupling. This process includes multiphase fluid seepage in porous media, thermal convection and conduction, gas hydrate dissociation, and the solid deformation of hydrate-bearing sediments. To establish a mathematical model describing the multi-physical field coupling involved in gas hydrate extraction, we made the following assumptions:

(1) The gas within the hydrates is pure methane and ice formation is neglected;
(2) Pressure change is considered the primary factor influencing gas hydrate dissociation in this study; deformation caused by temperature changes is not accounted for;
(3) The multiphase flow process follows Darcy's law and the formation is assumed to be a linearly elastic medium;
(4) All gas generated from gas hydrate dissociation is extracted through the borehole and gas hydrate dissociation is considered complete.

2.2. Mathematical Model

2.2.1. Energy Conservation Equation

Gas hydrate dissociation is an endothermic process; hence, temperature variation within the reservoir is a critical factor affecting gas hydrate extraction. Considering both thermal conduction and convection in the reservoir, the energy conservation equation during hydrate dissociation is expressed as follows:

$$\frac{\partial\left[\rho_w\gamma S_w C_w T+\rho_g\gamma S_g C_g T+\rho_h\gamma S_h C_h T+\rho_s(1-\varphi)C_s T\right]}{\partial t}+\nabla\cdot\left(\rho_w\gamma S_w v_{w,t}C_w T+\rho_g\gamma S_g v_{g,t}C_g T\right)=\nabla\cdot\lambda_{eff}\nabla T+Q_h \tag{1}$$

where ρ_w, ρ_g, ρ_h, ρ_s represent densities of the water phase, gas phase, hydrate, and sediment particles, respectively, in kg/m^3; S_w, S_g, S_h represent saturation of water, gas, and hydrate phases, respectively; C_w, C_g, C_h, C_s represent the specific heat capacities of the water phase, gas phase, hydrate, and sediment particles, respectively, in J/(kg·K); T represents the reservoir temperature, in K; $v_{w,t}$, $v_{g,t}$ represent the velocity of the water and gas phases, respectively, relative to the control volume, in m/s; λ_s, λ_g, λ_w, λ_h represent the thermal conductivities of sediment particles, gas, water, and hydrate phases, respectively, in W/(m·K); Q_h represents the latent heat of the phase transition for hydrate dissociation, in W/m^3; γ represents formation porosity; and t represents time, in s.

2.2.2. Seepage Field Equations

In gas hydrate-bearing formations, only gas and water are generally considered as mobile phases. According to the continuity equation and Darcy's law, the seepage equations for gas and water phases are presented as:

$$\nabla\left[\frac{K_{rg}K\rho_g}{\mu_g}\left(\nabla\rho_g+\rho_g g\right)\right]+m_g=\frac{\partial\left(\gamma\rho_g S_g\right)}{\partial t} \tag{2}$$

$$\nabla\left[\frac{K_{rw}K\rho_w}{\mu_w}\left(\nabla\rho_w+\rho_w g\right)\right]+m_w=\frac{\partial\left(\gamma\rho_w S_w\right)}{\partial t} \tag{3}$$

where K_{rg}, K_{rw} represent the relative permeabilities for the gas and water phases, respectively; K represents the absolute permeability of the porous sediment medium, in mD; μ_g, μ_w represent the viscosities of methane gas and the water phase, respectively, in Pa·s; m_g, m_w represent the production rates of gas and water per unit volume of dissociating hydrate, respectively, in kg/(m^3·s); and g represents the acceleration due to gravity, in m/s^2.

2.2.3. Gas Hydrate Dissociation Kinetics Model

This study uses the Kim–Bishnoi model, based on the pressure-driven dissociation mechanism [25]. According to this model, hydrate dissociation occurs in two stages: first, the destruction of the clathrate lattice on the particle surface, followed by the desorption of guest molecules from the surface. Therefore, the gas production rate, m_g, water production rate, m_w, and hydrate consumption rate, m_h, during hydrate dissociation are presented as follows:

$$m_g = k_{reac} M_{CH_4} A_{rs} (p_c - p_g) \tag{4}$$

$$m_w = m_g N_h \frac{M_{H_2O}}{M_{CH_4}} \tag{5}$$

$$m_h = -m_g \frac{M_h}{M_{CH_4}} \tag{6}$$

$$k_{reac} = k_d^0 \exp\left(\frac{-\Delta E_a}{RT}\right) \tag{7}$$

where m_h represents the dissociation rate of hydrate per unit volume, in kg/(m^3·s); k_{reac} represents the hydrate dissociation rate constant, in mol/(m^2·Pa·s); A_{rs} represents the surface area per unit volume of dissociating hydrate in the reservoir, in m^{-1}; p_c and p_g represent the capillary pressure and hydrate phase equilibrium pressure, respectively, in Pa; M_{CH4} represents the molar mass of methane gas, in kg/mol; M_{H2O} represents the molar mass of water, in kg/mol; M_h represents the molar mass of hydrate, in kg/mol; N_h represents the number of hydrates; k^o_d: 3.6 × 10^4, mol/(m^2·Pa·s); and $-\Delta E_a/RT$:9752.73K.

2.2.4. Absolute Permeability Model

To simplify the permeability calculations in the hydrate dissociation numerical model, we used the Hardwick absolute permeability model [26]. This model assumes that the permeability of hydrate-bearing formations remains at a sufficiently low value until the hydrate saturation reaches a specified level. The corresponding expression is as follows:

$$K = \begin{cases} K_c, S_h > S_{hc} \\ K_c + (K_0 - K_c)\left(\frac{S_{hc} - S_h}{S_{hc}}\right), \ 0 \le S_h \le S_{hc} \end{cases} \tag{8}$$

where K_0 represents the initial absolute permeability of the porous sediment medium, in mD; S_{hc} represents residual hydrate saturation; and K_c represents the permeability of the porous sediment medium when $S_h > S_{hc}$, in mD.

2.2.5. Relative Permeability Model

The relative permeability model employs the modified Brooks–Corey model, which is widely used for its simplicity and ease of solution [27]. Note that the relative permeabilities, n_w for water and n_g for gas, are empirical parameters obtained through experimental fitting. The corresponding expressions are:

$$p_g - p_w = p_c \tag{9}$$

$$K_{rg} = K_{rgo} S_{ges}^{n_g} \tag{10}$$

$$K_{rw} = K_{rwo} S_{wes}^{n_w} \tag{11}$$

$$S_{wes} = \frac{S_{we} - S_{wre}}{1 - S_{wre} - S_{gre}} \tag{12}$$

$$S_{ges} = \frac{S_{ge} - S_{gre}}{1 - S_{wre} - S_{gre}} \tag{13}$$

$$S_{we} = \frac{S_w}{1 - S_h} \tag{14}$$

$$S_{ge} = \frac{S_g}{1 - S_h} \tag{15}$$

$$S_{wre} = \frac{S_{wr}}{1 - S_h} \tag{16}$$

$$S_{gre} = \frac{S_{gr}}{1 - S_h} \tag{17}$$

where K_{rg} represents the relative permeability of the gas phase, in mD; K_{rw} represents the relative permeability of the water phase, in mD; S_{wr} represents irreducible water saturation; and S_{gr} represents irreducible gas saturation.

2.2.6. Latent Heat of the Phase Transition for the Hydrate Equation

According to Sun et al., the expression for the latent heat of the phase transition of hydrates is presented as follows [28]:

$$Q_h = \frac{m_h}{M_h}(B_1 - B_2 T) \tag{18}$$

where B_1 and B_2 represent coefficients related to the latent heat of the phase transition equation for hydrates.

2.3. Finite Element Model

Horizontal wells can significantly improve the production capacity of hydrate-bearing formations while notably reducing the risk of secondary hydrate formation. Therefore, this study focuses on analyzing the depressurization extraction of hydrates under various factors in the context of horizontal wells. The model used for the simulation is illustrated in Figure 2. The overall dimensions of the model are 70 m × 60 m × 60 m (length × width × height, respectively), and an unstructured tetrahedral mesh is used, with a denser mesh applied around the wellbore. Boundary conditions for the model are as follows: the perforated section of the well maintains a constant pressure throughout the simulation, corresponding to the extraction pressure; the left and right, as well as top and bottom boundaries of the formation, are assigned pressure boundaries equal to the initial formation pressure; and the front and back boundaries are set with constant pressure and temperature values equal to those of the formation. This setup provides a comprehensive framework to evaluate the stability and performance of hydrate extraction using horizontal wells under controlled depressurization conditions.

The initial depressurization extraction pressure was set at 5.0 MPa, with an initial pressure of 15 MPa and an initial temperature of 285 K in the hydrate-bearing formation. The wellbore radius was 0.25 m, and the completion method involved gravel packing. The perforated section had a length of 20 m. The physical properties of the hydrate used in the simulation are shown in Table 1.

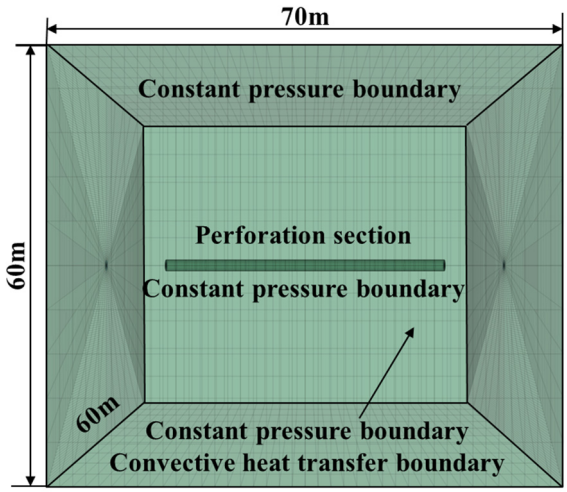


Figure 2. Schematic diagram of the hydrate buck mining model.

Table 1. Physical properties of the hydrate-bearing formation [29,30].

Parameter	Unit	Value	Parameter	Unit	Value
Wellbore radius	m	0.25	Gas specific heat capacity	J/(kg·K)	2180
Hydrate saturation	-	0.5	Water specific heat capacity	J/(kg·K)	4200
Gas saturation	-	0	Hydrate specific heat capacity	J/(kg·K)	2220
Water saturation	-	0.3	Formation particle specific heat capacity	J/(kg·K)	2180
Absolute permeability (without hydrate)	md	2.5	Hydrate thermal conductivity	W/(m·K)	2.0
Formation density	kg/m^3	2600	Sediment particle thermal conductivity	W/(m·K)	10
Porosity (without hydrate)	-	0.48	Water thermal conductivity	W/(m·K)	0.5
Gas thermal conductivity	W/(m·K)	0.06			
Hydrate relative permeability model	-	S_{wr} = 0.3, S_{gr} = 0.05, K_{wro} = 0.3, K_{gro} = 0.1, n_g = 4, n_w = 4			

3. Results and Discussion

During the depressurization and decomposition of hydrates, changes occur in the formation temperature, pore pressure, and other mechanical parameters. Therefore, for the stability analysis of hydrate production wellbores, it is crucial to understand the variations in pore pressure, temperature, hydrate saturation, and other key parameters throughout the hydrate decomposition process. This study focuses on examining the characteristics of hydrate decomposition under varying wellbore sizes, perforation lengths, extraction pressures, hydrate saturations, and permeabilities to provide data support for hydrate wellbore stability research. Additionally, the effects of these factors on reservoir and production parameters were analyzed to assess their impact on gas production from natural gas hydrates. These findings contribute to the selection of extraction areas and the design of extraction parameters for hydrate exploitation in the Shenhu area of the South China Sea.

3.1. Wellbore Effects

The depressurization method for hydrate extraction, which can induce hydrate decomposition without continuous stimulation, is regarded as one of the most promising and economically efficient methods for hydrate exploitation. However, this method has

the drawback of being prone to wellbore instability issues, such as bottomhole landslides. Although solid-state fluidization can mitigate the geological and environmental risks associated with subsurface hydrate decomposition, it often results in lower production rates. To address these issues, a study was conducted on hydrate decomposition characteristics under wellbore radii of 0.1 m, 0.25 m, and 0.5 m with a perforation interval of 20 m. These different wellbore sizes represent three extraction scenarios:

Scenario 1: A wellbore radius of 0.1 m simulating conventional wellbore depressurization extraction with an extraction pressure of 5 MPa.

Scenario 2: A wellbore radius of 0.25 m simulating a conventional wellbore expanded through solid-state fluidization, followed by depressurization extraction at the same pressure.

Scenario 3: A wellbore radius of 0.5 m, with extraction conditions similar to Scenario 2, designed to obtain data on pore pressure, temperature, and hydrate decomposition under large wellbore conditions. This scenario provides a basis for analyzing wellbore stability in large-diameter wells and offers insights into large-wellbore hydrate extraction.

The gas and water production rates over a 60-day period, as well as cumulative gas and water production, are shown in Figure 3. As illustrated in Figure 3a, the gas and water production rates gradually decrease over time, with a faster decline observed in the 0.5 m wellbore, though still higher than in the other scenarios. In the later stages, the production rates for the 1 m wellbore decrease steeply due to two main factors: (1) the production water from hydrate decomposition impedes pressure transmission, reducing formation pressure to the point where it can no longer support decomposition in the hydrate frontier region; and (2) hydrate decomposition reduces the formation temperature, shifting the hydrate equilibrium toward lower temperatures, while slow heat transfer in the formation fails to sustain the necessary heat for continued decomposition.

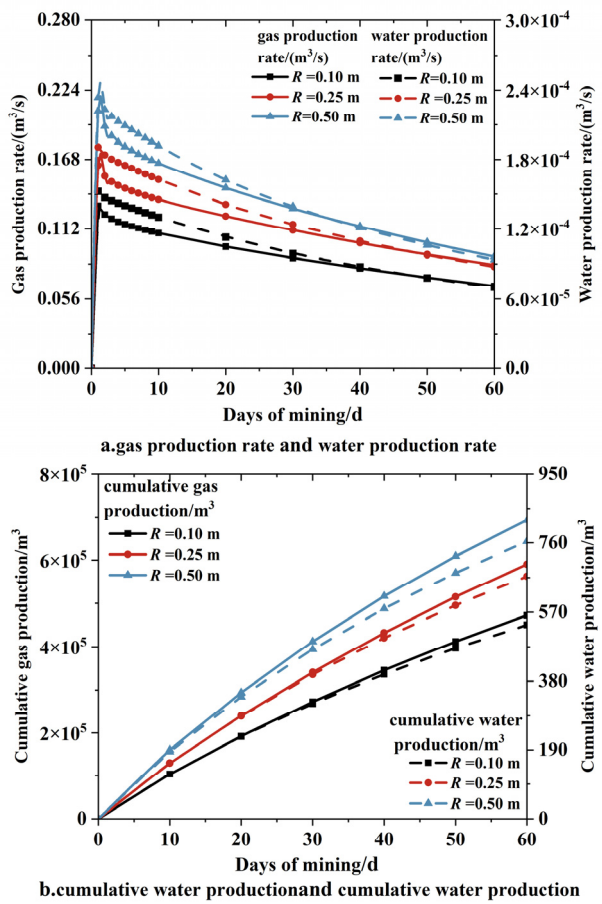


Figure 3. Gas and water production versus time over 60 days for different borehole diameters.

With increasing the wellbore size, the gas and water production rates significantly improve due to an enlarged contact area with the hydrate formation, increased drainage channels, and an enhanced hydrate decomposition rate. As shown in Figure 3b, cumulative gas and water production over the same timeframe rises with wellbore size. Scenario 1 achieves a cumulative gas production of 470,000 cubic meters, with an average daily gas output of 7800 cubic meters. Scenario 2 produces a cumulative 590,000 cubic meters of gas, averaging 9800 cubic meters per day. Scenario 3 reaches a cumulative gas production of 690,000 cubic meters, with an average daily production of 11,600 cubic meters, marking a 46% increase in formation productivity compared to Scenario 1. These results suggest that Scenario 3 significantly enhances formation productivity and may represent a promising new approach to hydrate exploitation.

The evolution of pore pressure over time under different wellbore radii is shown in Figure 4. From top to bottom, the figure displays the numerical simulation results for depressurization-driven hydrate extraction in formations with wellbore radii of 0.1 m, 0.25 m, and 0.5 m. Four time points—15 days, 30 days, 45 days, and 60 days (end of extraction)—are selected to represent early (15 days) and late (60 days) stages of extraction. As the hydrate extraction progresses, the formation pressure decreases outward from the wellbore, though the diffusion rate slows over time.

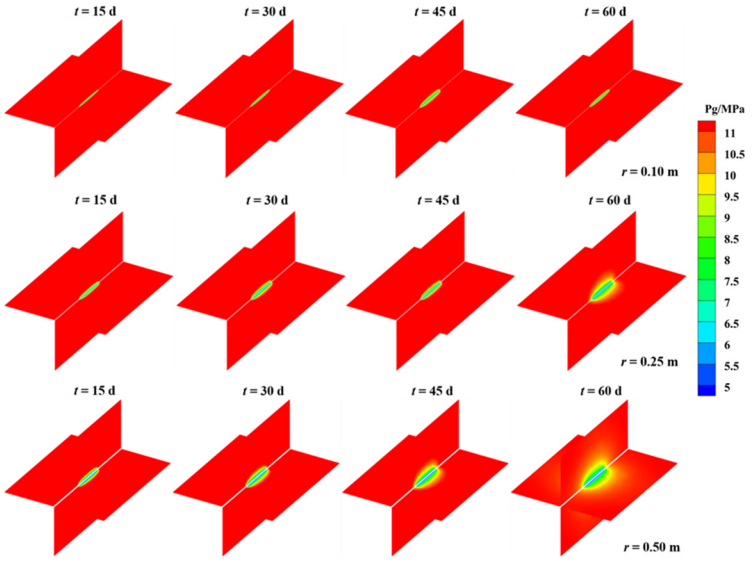


Figure 4. Spatial distribution and evolution of formation pore pressure at different borehole radii.

For example, with a 0.2 m wellbore, the depressurization front moves 0.40 m, 0.21 m, 0.22 m, and 0.11 m at 15-day intervals, with a total front movement of 0.94 m over 60 days. In the early extraction stages, the pressure difference between the formation and wellbore is highest, resulting in rapid depressurization. This process enhances formation permeability through hydrate decomposition, allowing the depressurization front to advance further. As the extraction continues, however, the pressure gradient between the formation and the wellbore diminishes, slowing the depressurization rate and front movement.

Smaller wellbore sizes are less favorable for gas flow from the formation into the wellbore, and the decomposing gas may cause blockages within the wellbore over time, raising the wellbore pressure and inhibiting further hydrate decomposition. By contrast, for a 1 m wellbore, the depressurization front moves 3.1 m in the same period, indicating that a larger wellbore enhances the movement of the depressurization front. This increased depressurization distance results from the enlarged contact area between the wellbore and hydrate-bearing formation when the perforation length is held constant, effectively expanding the depressurized area. Consequently, the formation response is more pronounced with

larger wellbores, characterized by faster pressure propagation (Figure 4), more extensive cooling around the well (Figure 5), and increased hydrate decomposition (Figure 6).

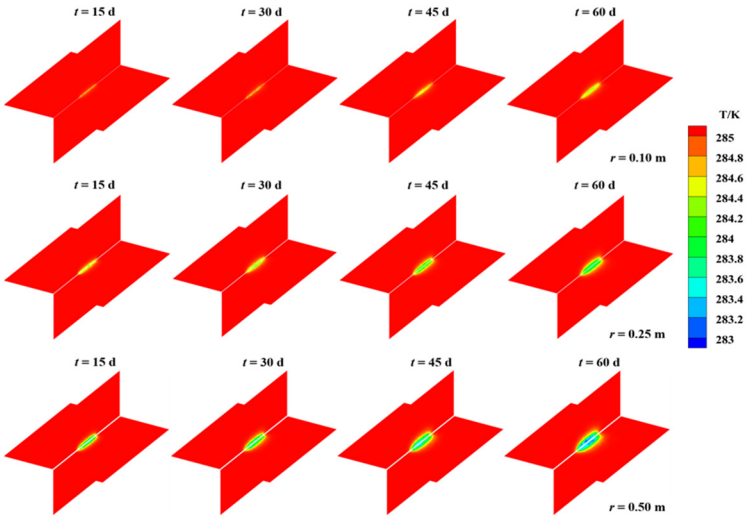


Figure 5. Spatial distribution and evolution of formation temperature at different borehole radii.

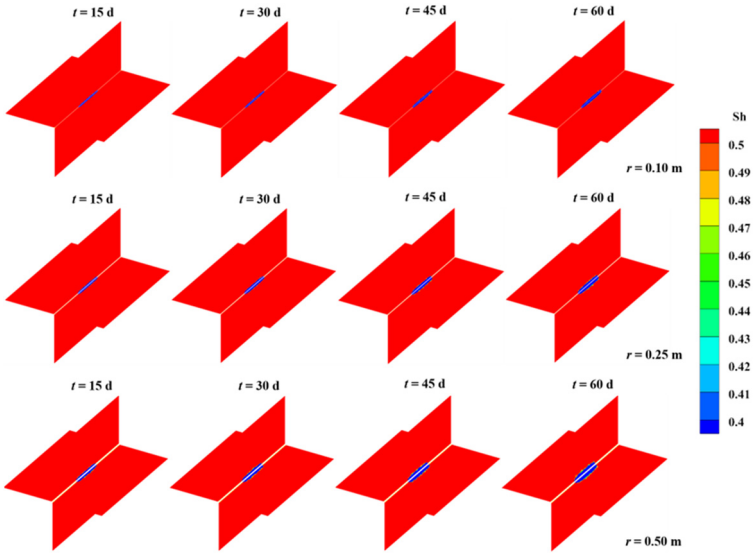


Figure 6. Spatial distribution and evolution of hydrate saturation at different borehole radii.

The evolution of formation temperature under various wellbore sizes is illustrated in Figure 5. The formation temperature declines outward from the wellbore, with heat transferring from the surrounding area toward the wellbore. For a wellbore radius of 0.1 m, after 15 days of extraction, most of the hydrate-bearing formation remains near 285 K, with only a small area showing minor temperature changes, indicating limited hydrate decomposition. As the extraction time increases, the cooling area gradually expands, but the temperature remains unchanged in areas further from the wellbore. This stability suggests that reduced pore pressure is insufficient to induce hydrate decomposition in distant regions.

When comparing hydrate temperature changes across different wellbore radii at the same extraction time, the cooling region expands with increasing wellbore size. At 60 days, for instance, with a 0.1 m wellbore radius, the cooling front is approximately 1 m from the wellbore, with a minimum temperature of around 284 K—a reduction of only 1 K. However, for a 0.5 m wellbore, the cooling front extends approximately 3 m, with minimum temperatures around 283 K or lower. This trend indicates that larger wellbores

enhance the hydrate decomposition rate, leading to greater temperature changes in the formation within the same extraction time.

Figure 6 illustrates the evolution of hydrate saturation over time. During depressurization, the gas hydrate saturation near the wellbore gradually decreases, decomposing outward along the pressure gradient and forming a hydrate decomposition front. Comparing saturation distribution maps at the same extraction times for different wellbore radii, it is evident that the decomposition region expands as the wellbore size increases. For instance, in early extraction stages, with a wellbore radius of 0.1 m, no clear decomposition front is observed, with a decomposition radius of approximately 0.3 m (300% of the wellbore radius). In contrast, for a 0.5 m wellbore, the decomposition front begins to form with a radius of about 2 m (400% of the wellbore radius), demonstrating that larger wellbores can accelerate hydrate decomposition.

The hydrate decomposition region correlates positively with the wellbore size. For a 0.1 m radius wellbore, serving as a control, the decomposition area increases significantly over 60 days as the wellbore radius increases. When the radius expands to 0.25 m (150% increase), the decomposition region (dark-blue area) grows by 25%. At a radius of 0.5 m (400% increase), the decomposition area increases by 133%.

In conclusion, with larger wellbores, the formation experiences more significant changes in pore pressure, temperature, and hydrate saturation, suggesting that large wellbores can enhance hydrate productivity by enlarging the decomposition area and facilitating gas and water drainage. Therefore, the depressurization method may benefit from enlarging conventional wellbores using solid-state fluidization techniques before extraction to optimize hydrate extraction efficiency.

3.2. Perforation Interval Length

The research by Cao et al. indicates that single, vertical, well depressurization methods are unlikely to meet the demands for commercial gas hydrate extraction [31]. Consequently, complex well types, like horizontal wells and multilateral wells, are expected to play an irreplaceable role in the commercial exploitation of gas hydrates. Although the high completion costs and technical challenges of horizontal wells limit their use, China's second hydrate trial in the South China Sea included a horizontal well, demonstrating their effectiveness in increasing hydrate decomposition by expanding the contact area between the well and hydrate reservoir.

In this section, we examine hydrate decomposition characteristics under varying perforation interval lengths.

Figure 7 presents the changes in gas and water production rates over 60 days for different perforation interval lengths (20 m, 30 m, and 40 m), as well as cumulative gas and water production. As shown in Figure 7a, gas and water production rates rise rapidly at the beginning of extraction for each perforation length, then gradually decline over time, eventually stabilizing in a fluctuating state. Initially, as bottomhole depressurization begins, the hydrate system approaches its phase equilibrium boundary, causing equilibrium to destabilize. The resulting pressure gradient from the formation toward the wellbore becomes the main driver of hydrate decomposition. However, as hydrate decomposition progresses, pressure equalizes, reducing the gradient and causing a drop in the decomposition rate. Later in the extraction process, the pressure gradient between the hydrate-bearing formation and wellbore is insufficient to sustain hydrate decomposition, making formation heat the primary driver. Since heat transfer within the formation depends on its thermal properties, hydrate decomposition slows.

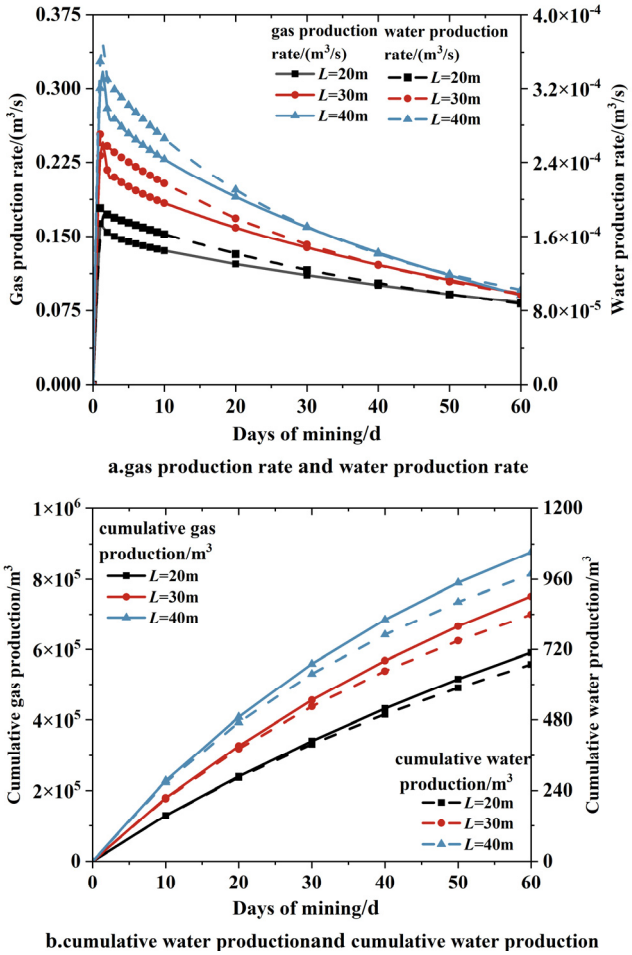


Figure 7. Gas and water production versus time over 60 days for different shot hole section lengths.

From Figure 7b, which shows cumulative gas and water production over 60 days, we observe that a 20 m perforation interval produces 590,000 m^3 of gas. Extending the interval to 30 m increases cumulative gas production by 160,000 m^3, yielding 750,000 m^3. However, further increasing the interval to 40 m adds only 130,000 m^3 of gas, suggesting diminishing returns. Thus, an optimal horizontal length likely exists that maximizes incremental production. In the late stages of extraction, cumulative gas and water production curves level off due to the limited heat available for hydrate decomposition.

To enhance the decomposition rates during late extraction, heat injection into the formation could be explored. Raising the formation temperature could serve as an auxiliary measure to boost hydrate decomposition, thereby increasing the gas yield.

Figure 8 illustrates the temporal and spatial evolution of formation pore pressure under varying perforation interval lengths. As extraction progresses, the formation pressure decreases, with the pressure diffusion zone expanding in tandem with the perforation interval length. According to the figure, after 60 days of extraction at a 20 m perforation interval, the pressure reduction zone around the well resembles that seen after 45 days at a 40 m interval. Similarly, the pressure distribution pattern at a 40 m interval after 60 days matches that observed at 45 days with a 60 m perforation interval. This trend suggests that each 20 m increase in the perforation length improves the pressure drawdown rate by roughly 25%, holding other factors constant.

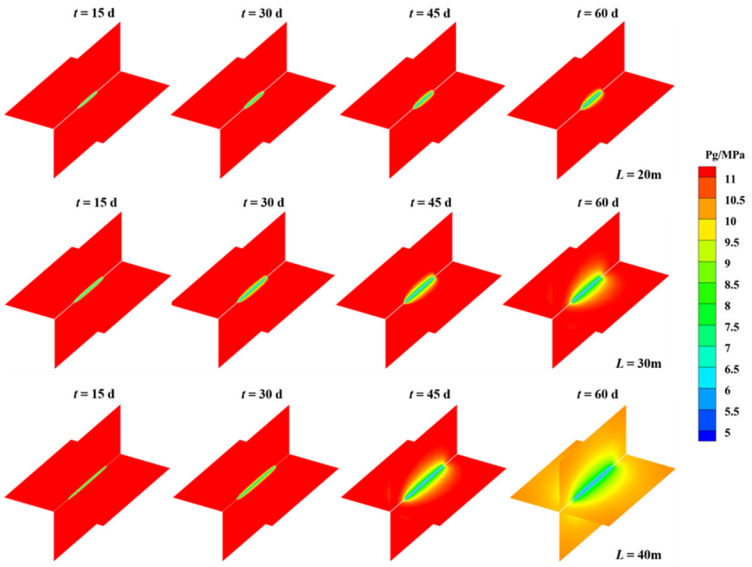


Figure 8. Spatial distribution and evolution of pore pressure in formations with different shot hole sections.

After 60 days of extraction, the overall pressure within the formation with a 20 m perforation interval remains above 11 MPa, with a drawdown magnitude of 3–4 MPa and a rate of 0.05–0.06 MPa/day. Under a 40 m interval, the majority of the formation exhibits pressure levels in the range of 8–10 MPa, with a drawdown magnitude of 5–7 MPa and a rate of 0.08–0.11 MPa/day. Thus, both the drawdown magnitude and rate increase with extended perforation lengths. Therefore, when extracting hydrates through depressurization, extending the perforation interval length enhances the drawdown efficiency, thereby improving the overall hydrate extraction rates.

Figure 9 shows the evolution of formation temperature over time for varying perforation lengths. Temperature trends are consistent across different intervals, with a gradual decrease initially, followed by a more rapid drop in later extraction stages. At a 20 m interval, for instance, only the area near the wellbore shows a temperature drop after 15 days, while a more significant cooling zone emerges by 45 days. In the early stages, the pressure difference between the wellbore and formation drives hydrate decomposition, with the formation heat supplementing this process. As extraction proceeds, the pressure differential energy depletes, leaving the formation heat as the main energy source for decomposition. Increasing the perforation length accelerates this shift: for example, notable differences in cooling zones are observed between 15 and 30 days with a 40 m interval, while the temperature in remote areas remains largely unchanged due to low thermal conductivity. While the cooling area expands with the perforation length, the relationship is not strictly linear because hydrate decomposition is a complex physicochemical process that warrants a deeper investigation.

Figure 10 shows the changes in hydrate saturation over time for various perforation lengths. As extraction proceeds, the hydrate saturation near the wellbore gradually decreases, expanding in an arc-like shape outward, with the center experiencing the fastest decomposition rate. This pattern indicates that pressure distribution is the main determinant of hydrate decomposition area. With an increased perforation length, the decomposition rate rises, enlarging the affected zone. After 60 days, a distinct hydrate decomposition front is visible with a 40 m perforation length, while other conditions show less pronounced fronts. This effect arises because a longer perforation interval expands the depressurization area, thereby impacting a larger hydrate region. Hydrate decomposition further aids pressure transmission, creating a positive feedback loop.

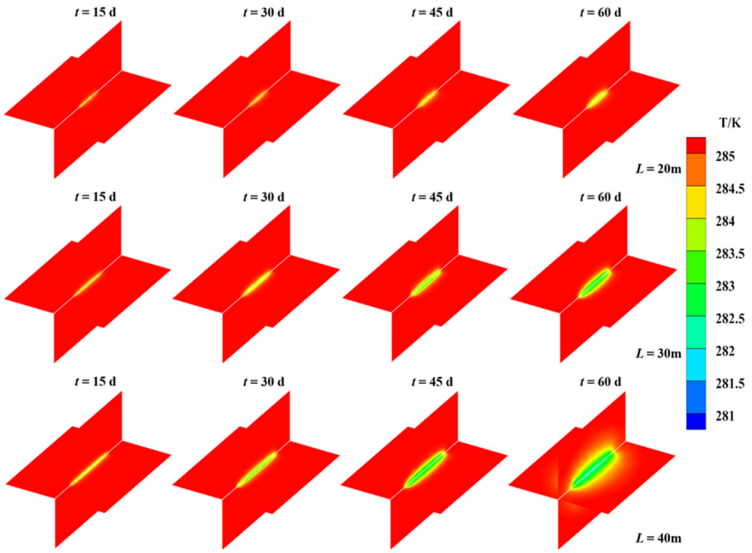


Figure 9. Spatial distribution and evolution of formation temperature in different shot hole sections.

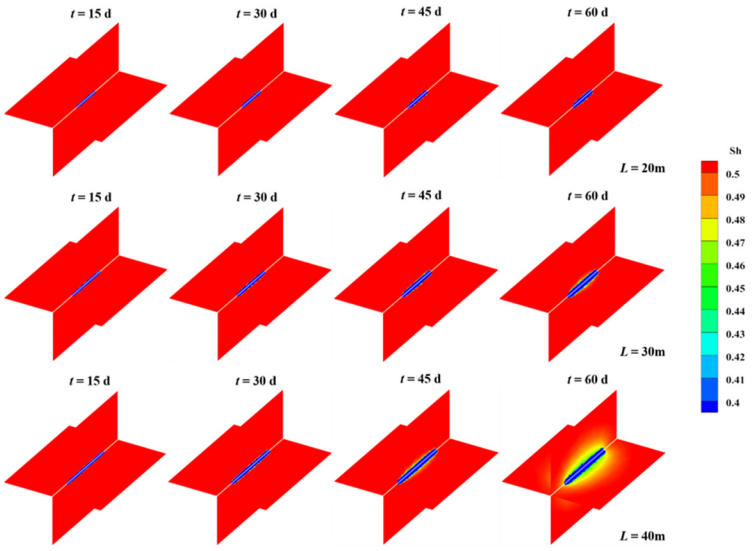


Figure 10. Spatial distribution and evolution of hydrate saturation in different shot hole sections.

To validate this observation, a comparison of the pressure front position in Figure 8 with the hydrate decomposition front in Figure 10 after 60 days reveals a minimal difference, both located approximately 12.5 m from the wellbore axis. The region where hydrate saturation (Sh) is below 40% (depicted in blue) lies in the range of 1.5–2.5 m of the wellbore axis, with a modest increase in this area as the perforation length increases. The shape and area of the blue region in the saturation map also align with the cooling area in Figure 9. This confirms that, in the early stages of decomposition, the pressure differential serves as the primary energy source influencing the formation of the hydrate front, while formation heat later governs the size of the decomposed region as the process continues.

3.3. Production Pressure

Currently, depressurization is widely regarded as the most promising method for gas hydrate extraction. In this approach, the production wellbore is positioned within or below the hydrate layer, disrupting the hydrate's equilibrium state and inducing destabilization and decomposition. This section examines how varying production pressures impact

formation pore pressure, temperature, and hydrate saturation, setting the groundwork for analyzing wellbore stability in hydrate extraction.

Figure 11 illustrates the impact of different production pressures (Pw) on gas and water production rates (Figure 11a) and cumulative production volumes (Figure 11b) over 60 days. Based on the hydrate phase diagram and formation temperature, Pw values are set at 4 MPa, 5 MPa, and 6 MPa, with other conditions remaining constant. During depressurization extraction, the pressure differential acts as the main driving energy for hydrate decomposition. As shown in Figure 11a, a lower Pw significantly enhances gas and water production rates. When Pw decreases from 6 MPa to 4 MPa, the average gas production rate over 60 days increases by approximately 23%, while the water production rate rises by around 11.3%. This finding suggests that production pressure has a more substantial effect on gas output than on water production.

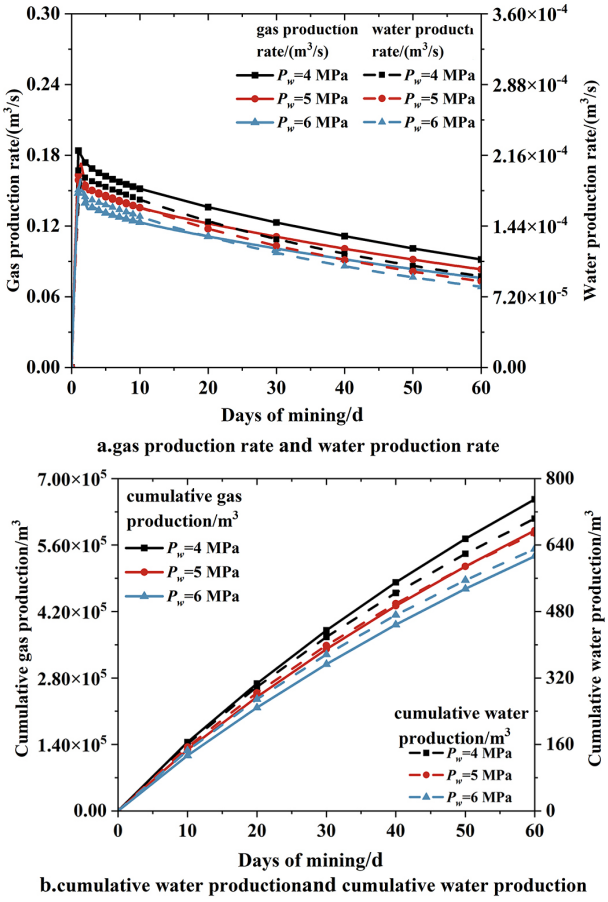


Figure 11. Gas and water production versus time over 60 days for different production pressures.

To further verify this, a gas-to-water ratio (GWR) analysis was conducted. The results show that, at lower Pw values, the GWR is initially low but rises before gradually declining as extraction continues. In contrast, the GWR under higher Pw conditions remains relatively stable at first, eventually mirroring the trend seen at lower Pw values. This pattern reinforces the conclusion that lower Pw enhances gas production efficiency.

As shown in Figure 11b, cumulative gas and water production across the three production pressures follow similar trends over time: they initially increase rapidly but approach stability as depressurization proceeds, indicated by a reduction in the slope of the curves. This pattern aligns with previously observed behaviors and will not be elaborated on further here. Under a production pressure of 6 MPa, the cumulative gas output over 60 days reaches 530,000 cubic meters. Reducing Pw by 1 MPa increases total gas production

by approximately 10.25%, while a 2 MPa reduction leads to a 23.05% increase. Therefore, maintaining a lower wellbore pressure during depressurization is essential for maximizing hydrate production.

Using a baseline production pressure of Pw = 5 MPa, we can analyze the formation pressure distribution by increasing and decreasing Pw by 1 MPa (6 MPa and 4 MPa, respectively). Figure 12 illustrates the spatial distribution of hydrate saturation and its evolution throughout the extraction process at various pressures. In the vicinity of the wellbore, pressures are generally around 7–8 MPa, with a visible pressure front in all cases. However, the depressurization zone is notably larger at Pw = 4 MPa than at 6 MPa. This discrepancy is primarily due to the greater pressure differential at lower production pressures, which facilitates a larger hydrate decomposition zone and accelerates pressure diffusion. Under identical conditions, a lower production pressure results in a more significant reduction in the formation pressure and an increased depressurization rate. For instance, the maximum formation pressures recorded are 12.25 MPa at Pw = 4 MPa, 12.48 MPa at Pw = 5 MPa, and 12.97 MPa at Pw = 6 MPa. These values suggest that Pw has a noticeable impact on distant formation pressures, albeit not a substantial one.

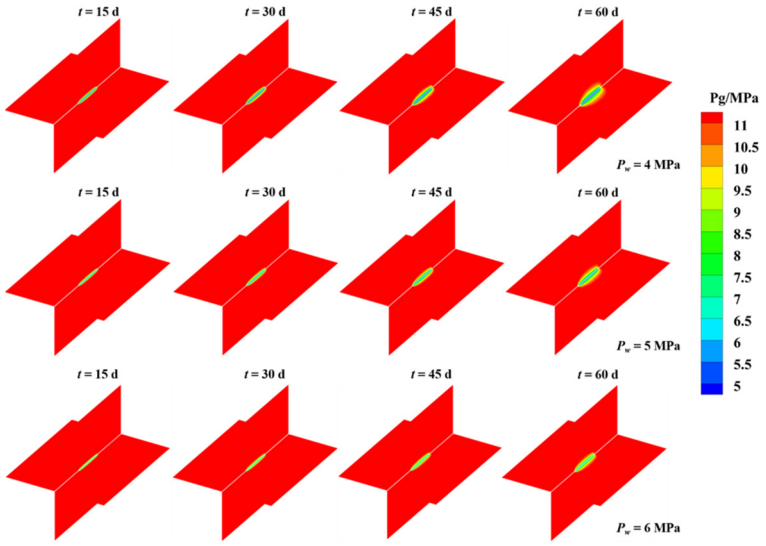


Figure 12. Spatial distribution and evolution of formation pore pressure under different production pressures.

As shown in Figure 13, the spatial distribution and evolution of formation temperature exhibit a staircase-like pattern across different production pressures, with the temperature decreasing progressively along the vertical direction of the wellbore. Comparing identical extraction times, the low-temperature zone is both more extensive and colder at Pw = 4 MPa than at 6 MPa. After 60 days of extraction, the minimum temperature near the wellbore reaches approximately 283 K at Pw = 4 MPa, compared to around 284 K at Pw = 6 MPa. This outcome arises because the initial formation temperatures are the same; however, more extensive hydrate decomposition at Pw = 4 MPa results in lower temperatures.

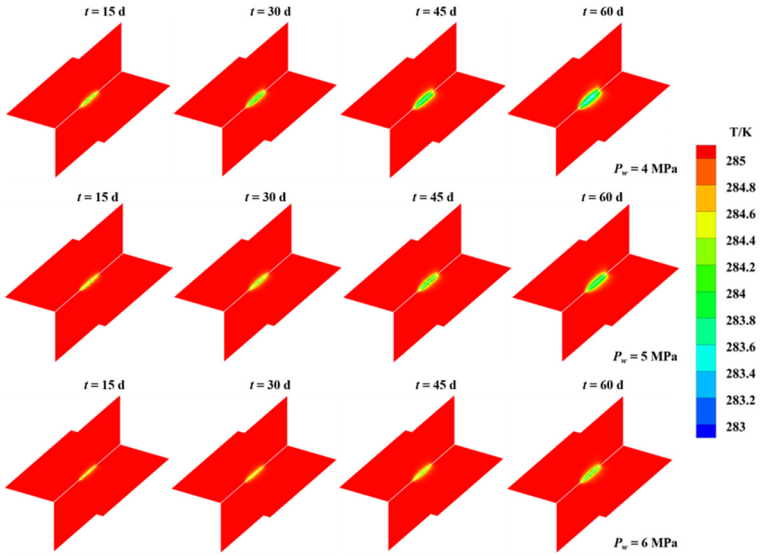


Figure 13. Spatial distribution and evolution of formation temperatures at different production pressures.

As depicted in Figure 14, hydrate decomposition increases with ongoing extraction, and lower production pressures result in a more extensive decomposition region. Under a Pw of 6 MPa, the hydrate decomposition radius is approximately 4.8 times the wellbore radius (0.25 m), expanding to about six times at Pw = 5 MPa, and roughly eight times at Pw = 4 MPa. These results highlight that reducing Pw and thereby enhancing the pressure differential between the formation and the wellbore significantly increases the area of hydrate decomposition, leading to higher gas production. However, lower Pw carries the risk of formation sand production and instability, as an expanded hydrate decomposition zone creates a larger unstable region within the formation, ultimately weakening it. Therefore, actual extraction should consider formation characteristics to select an optimal Pw, ensuring both effective and stable hydrate extraction.

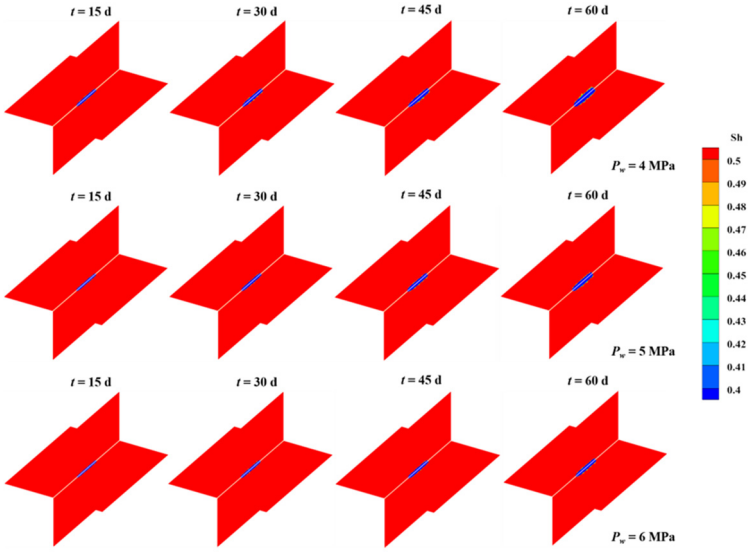


Figure 14. Spatial distribution and evolution of hydrate saturation at different extraction pressures.

3.4. Hydrate Saturation Effect

Exploiting formations with high hydrate saturation can be economically advantageous, but the presence of hydrates slows the pressure transmission within the reservoir. Additionally, hydrate decomposition under varying saturation levels influences the temperature

distribution across the formation. In this section, we examine hydrate depressurization and extraction characteristics at different saturation levels: Sh = 30%, Sh = 40%, and Sh = 50%.

As illustrated in Figure 15a, the production rates of gas and water over a 60-day period differ based on hydrate saturation. For lower saturation levels, the gas and water production rates decline rapidly, while for higher saturation levels, these rates remain relatively stable. In formations with low hydrate saturation, pressure transmission is faster, and the rapid initial decomposition of hydrates causes a quick temperature drop. Consequently, there is less hydrate decomposition at later stages, leading to a stabilization of gas and water production rates. Surprisingly, as shown in Figure 15b, cumulative gas and water production are lower in high-saturation formations than in low-saturation formations. For example, cumulative gas production after 60 days is 0.59 million cubic meters at Sh = 50% but reaches 2.1 million cubic meters at Sh = 30%.

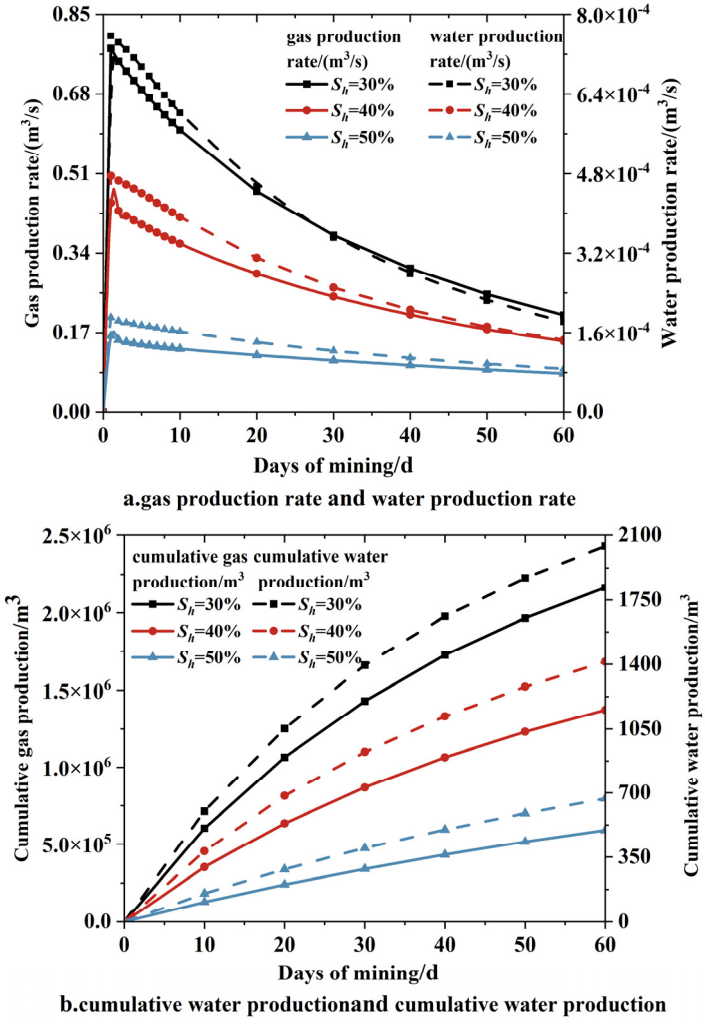


Figure 15. Gas and water production versus time over 60 days at different hydrate saturation levels.

This trend is primarily due to the higher porosity in low-saturation formations, which facilitates faster pressure transmission and creates unobstructed pathways for gas flow toward the wellbore. Consequently, lower-saturation hydrate formations yield higher cumulative gas and water volumes over the same period.

Figure 16 illustrates how the formation pore pressure evolves over time with varying hydrate saturations. At a given time, pressure propagation in a formation with 30% hydrate saturation (Sh = 30%) is markedly faster than that in a formation with 50% saturation (Sh = 50%). After 60 days, the low-pressure zone (green region) in Sh = 30% extends

radially (rd) up to 5 m along the vertical wellbore direction, approximately 10 times the wellbore diameter, with visible pressure transmission lines reaching deeper into the formation. This difference can be attributed to the higher porosity and permeability in the Sh = 30% formation, which facilitates the rapid expulsion of water generated by hydrate decomposition and the existing pore fluids in the formation, thereby allowing pressure transmission into the deeper layers.

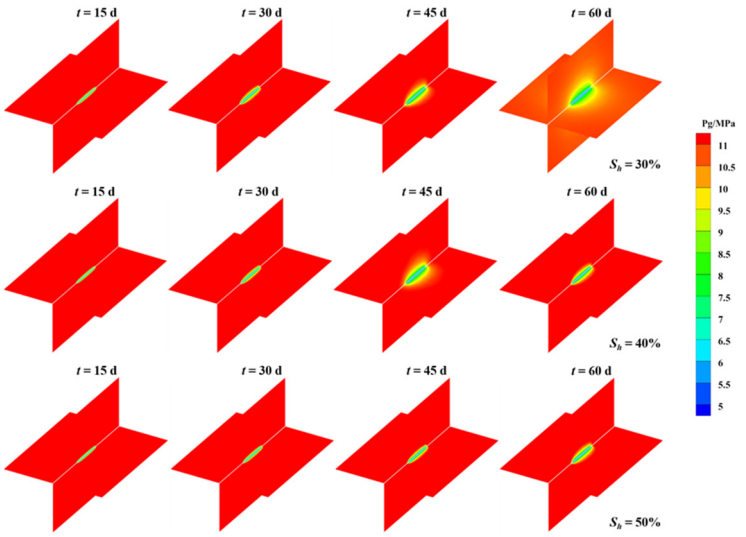


Figure 16. Spatial distribution and evolution of formation pore pressure at different hydrate saturations.

Conversely, in the Sh = 50% formation, the low-pressure zone (Rd) only reaches around 2 m, about four times the wellbore diameter, with a minimal pressure impact on the distal formation. This can be explained by the higher hydrate content, which introduces more solid hydrate phases within the formation, reducing the porosity and inhibiting fluid movement toward the wellbore, thus significantly impeding pressure propagation.

Figure 17 shows the temperature distribution over time for varying hydrate saturations. The Sh = 50% formation experiences slower cooling, with the temperature near the wellbore remaining around 284 K after 60 days. In contrast, the Sh = 30% formation shows a larger low-temperature region (blue zone) near the wellbore, reaching about five times the wellbore diameter. This discrepancy arises because lower-saturation formations experience more complete and thorough hydrate decomposition over the same period.

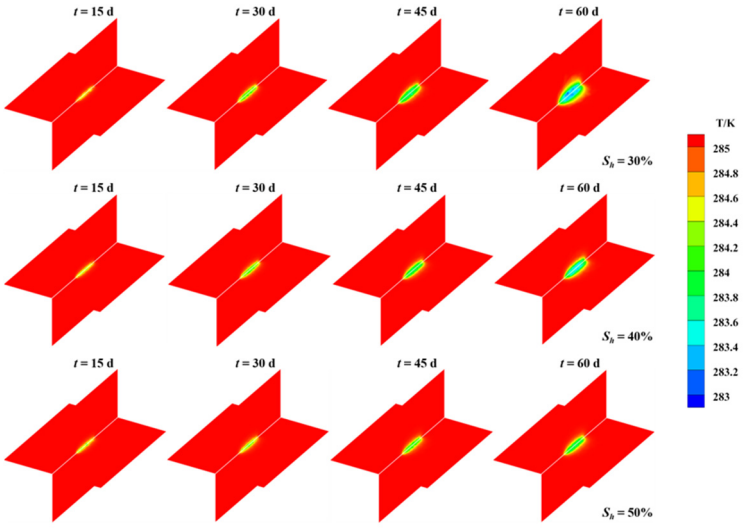


Figure 17. Spatial distribution and evolution of formation temperatures at different hydrate saturations.

A notable observation is the two-phase temperature decline over time during hydrate extraction: initial gradual cooling, followed by a more rapid drop later on. For instance, in the Sh = 30% formation, the temperature only drops by 0.4 K in limited areas during the first 15 days. However, between 45 and 60 days, the cooling area doubles, with a temperature drop of around 1 K. In the initial stages, pressure differential primarily drives hydrate decomposition, while in later stages, heat from the formation increasingly contributes, transmitting thermal energy to the low-temperature zone. As extraction continues, this two-stage thermal response results in a steady initial temperature drop followed by accelerated cooling.

Figure 18 displays the spatial distribution and temporal evolution of hydrate saturation. As anticipated, at the same time intervals, lower-saturation formations exhibit a larger hydrate decomposition zone (blue region), with a radius of approximately 2 m, compared to about 1.5 m in high-saturation formations. Combined with Figure 16, it is evident that lower-saturation formations have higher porosity and faster pressure transmission, which accelerates decomposition rates and expands the decomposition region.

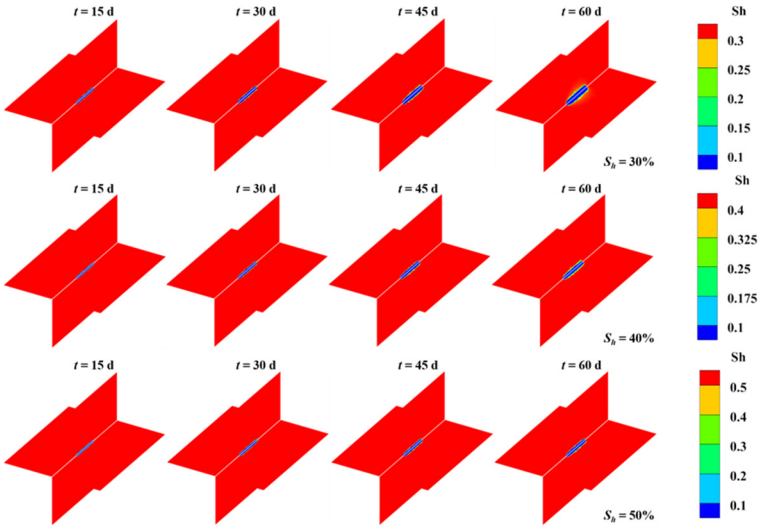


Figure 18. Spatial distribution and evolution of hydrate saturation at different hydrate saturation levels.

3.5. Permeability

Permeability varies significantly across different marine hydrate reservoirs. This section examines hydrate depressurization under permeability conditions of 1.0 mD, 1.5 mD, and 2.0 mD.

Figure 19a shows the gas and water production rates over 60 days for different permeabilities. The peak gas production rate increases with higher permeability (k), as higher permeability enables faster pressure transmission and more extensive hydrate decomposition. When k increases from 1.0 mD to 1.5 mD, the gas production rate rises by 37.67% and the water production rate by 36.11%. When k increases from 1.5 mD to 2.0 mD, gas production rises by 22.41% and water production by 22.09%. These results suggest that, while permeability significantly boosts production rates, the increase is not strictly linear.

Notably, gas and water production rates decline more quickly in high-permeability formations. In formations with a permeability of 2.0 mD, production rates drop more noticeably during the later stages of extraction than in 1.5 mD formations. This is due to the rapid depletion of energy as hydrates decompose quickly in high-permeability reservoirs without sufficient energy replenishment. Thus, during the later stages of production, additional energy sources (e.g., reducing wellbore pressure or injecting heat) should be considered to sustain hydrate decomposition and maintain production.

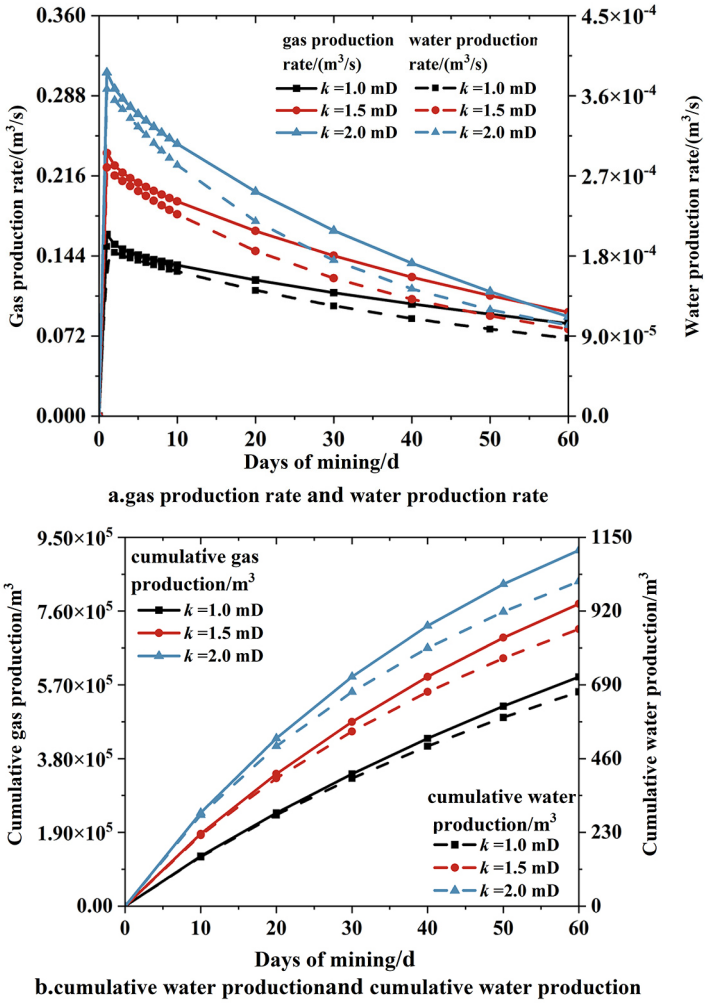


Figure 19. Gas and water production versus time over 60 days under different formation permeability conditions.

The cumulative gas and water production trends (Figure 19b) align with those observed for production rates (Figure 19a). Higher formation permeability enhances the total gas and water output. Specifically, increasing k from 1.0 mD to 1.5 mD raises cumulative gas production by 27.51%, and from 1.5 mD to 2.0 mD by 23.40%. In low-permeability reservoirs, fracturing techniques can be employed to increase reservoir permeability, which, when combined with depressurization methods, can optimize gas production from hydrate-bearing formations.

However, high permeability also correlates with increased water production. When k is increased from 1.0 mD to 2.0 mD, cumulative water production rises by 25.98%, indicating a 25% increase over initial values. Gas-to-water ratios calculated under different permeabilities show that higher permeability tends to reduce the gas-to-water ratio, signifying that the increase in water production outpaces the growth in gas production.

Figure 20 illustrates the pore pressure distribution and its evolution in formations with varying permeabilities. As permeability (k) increases, fluid migration accelerates, facilitating pressure drawdown transmission deeper into the formation, resulting in a more pronounced depressurization effect. Higher-permeability formations (k = 2.0 mD) display a broader low-pressure zone around the wellbore, while lower-permeability formations (k = 1.0 mD) exhibit a more localized pressure drop. In the later stages of production, it is notable that the wellbore pressure in high-permeability formations stabilizes at around 7–8 MPa. Coupled with corresponding wellbore temperatures of approximately 283 K

(shown in Figure 21), this explains the reduced gas and water production rates in the later stages, as the pressure and temperature become insufficient to sustain continued hydrate dissociation.

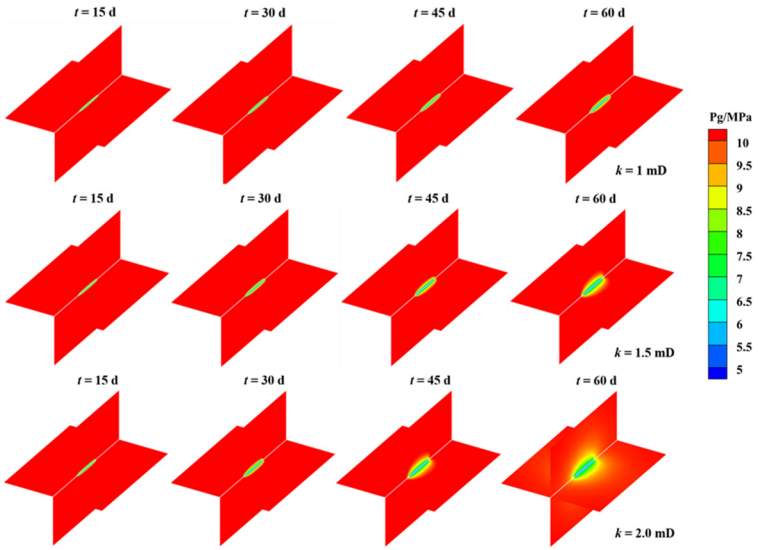


Figure 20. Spatial distribution and evolution of formation temperature at different formation permeabilities.

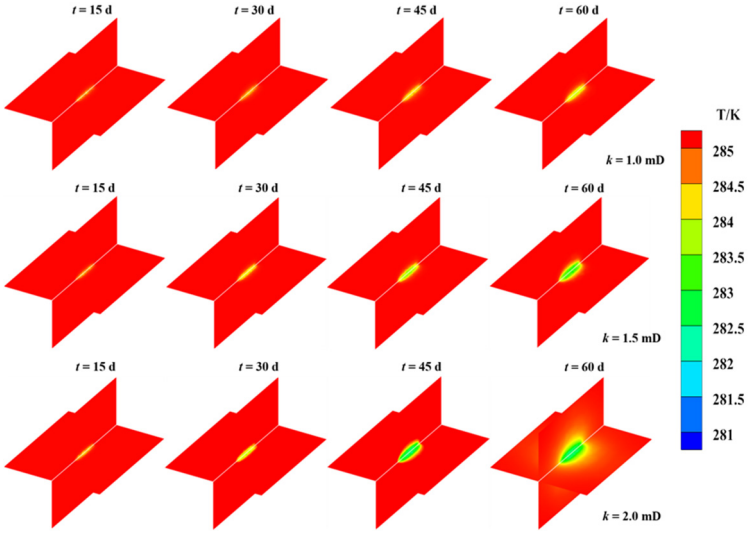


Figure 21. Spatial distribution and evolution of hydrate saturation under different formation permeabilities.

As shown in Figure 21, the temperature trends align with expectations. Early in production, the low-temperature zone primarily surrounds the depressurization segment near the perforated interval. Over time, this low-temperature region extends in a wave-like pattern into the reservoir. Increased permeability leads to a larger area experiencing temperature decline, as higher permeability promotes more extensive hydrate decomposition. The decomposition process absorbs heat from the surrounding formation, resulting in lower temperatures.

Figure 22 depicts the changes in hydrate saturation over time. Hydrate dissociation predominantly occurs near the depressurization section, with the dissociation front advancing in the same direction as pressure transmission. In formations with k = 1.0 mD, the dissociation front is less apparent. However, for k = 1.5 mD and k = 2.0 mD, both the

dissociation front and the size of the dissociation zone become more pronounced. This suggests that increased permeability not only enhances fluid movement and accelerates pressure diffusion, but also facilitates faster heat transfer from the undissociated zone to the dissociation zone. This results in a quicker temperature recovery after initial drops, supporting continued hydrate dissociation.

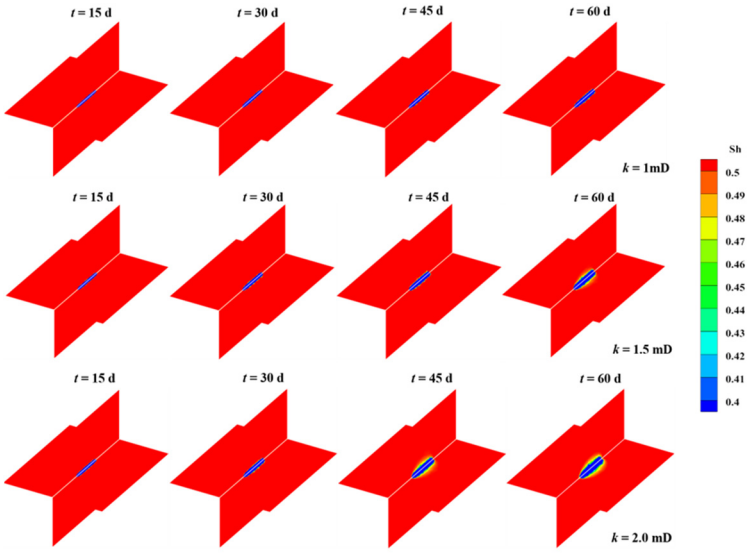


Figure 22. Spatial distribution and evolution of formation pore pressure under different formation permeability conditions.

4. Conclusions

This comprehensive analysis underscores the multifaceted nature of methane hydrate production, emphasizing the interplay between production pressure, hydrate saturation, and permeability. The findings illustrate how these factors collectively influence production rates, thermal dynamics, and pressure transmission within the reservoir.

(1) Lowering the production pressure enhances gas and water production rates by increasing the pressure differential. Lower hydrate saturation leads to faster pressure propagation and higher initial production rates due to higher porosity and permeability. High-saturation reservoirs, however, may maintain production over extended periods as pressure transmission improves with time. Higher permeability facilitates rapid pressure transmission and initial hydrate decomposition but results in quicker depletion of energy and resources, leading to lower production rates over time without external energy supplementation.

(2) The large wellbores and the long perforation interval can enhance hydrate productivity by enlarging the decomposition area and facilitating gas and water drainage. The depressurization method may benefit from enlarging conventional wellbores using solid-state fluidization techniques before extraction or increase the length of the perforation interval to optimize hydrate extraction efficiency.

(3) In the process of hydrate mining, formation temperature is the most critical factor in maintaining gas production, suggesting the timely reheating of the formation during hydrate mining.

Author Contributions: Methodology, Y.Z.; Validation, Y.H.; Resources, Y.Z.; Writing—original draft, Y.C.; Writing—review & editing, S.S. All authors have read and agreed to the published version of the manuscript.

Funding: This research was funded by the National Key R&D Program of China: 2021YFC2800905, and National Natural Science Foundation of China: U22244223.

Data Availability Statement: The original contributions presented in this study are included in the article. Further inquiries can be directed to the corresponding authors.

Conflicts of Interest: Yunjian Zhou, Yufa He, and Yu Chen are employed by the CNOOC Research Institute Co., Ltd. The remaining authors declare that this research was conducted in the absence of any commercial or financial relationships that could be construed as a potential conflict of interest.

References

1. Makogon, Y.F. Natural Gas Hydrates—A Promising Source of Energy. *J. Nat. Gas Sci. Eng.* **2010**, *2*, 49–59. [CrossRef]
2. Boswell, R.; Collett, T.S. Current Perspectives on Gas Hydrate Resources. *Energy Environ. Sci.* **2011**, *4*, 1206–1215. [CrossRef]
3. Li, Y.; Peng, G.; Tang, J.; Zhang, J.; Zhao, W.; Liu, B.; Pan, Y. Thermo-Hydro-Mechanical Coupling Simulation for Fracture Propagation in CO_2 Fracturing Based on Phase-Field Model. *Energy* **2023**, *284*, 128629. [CrossRef]
4. Song, Y.; Yang, L.; Zhao, J.; Liu, W.; Yang, M.; Li, Y.; Liu, Y.; Li, Q. The Status of Natural Gas Hydrate Research in China: A Review. Renew. Sustain. *Energy Rev.* **2014**, *31*, 778–791. [CrossRef]
5. Lijith, K.P.; Malagar, B.R.C.; Singh, D.N. A Comprehensive Review on the Geomechanical Properties of Gas Hydrate Bearing Sediments. *Mar. Pet. Geol.* **2019**, *104*, 270–285. [CrossRef]
6. Max, M.D.; Cruickshank, M.J. Extraction of Methane from Oceanic Hydrate System Deposits. In Proceedings of the Offshore Technology Conference, Houston, TX, USA, 3–6 May 1999; Volume 1, pp. 71–78. [CrossRef]
7. Gupta, A.; Aggarwal, A. Gas Hydrates Extraction by Swapping-Depressurisation Method. In Proceedings of the Offshore Technology Conference-Asia, Kuala Lumpur, Malaysia, 25–28 March 2014; Volume 2, pp. 1299–1304. [CrossRef]
8. Li, Y.; Hubuqin; Wu, J.; Zhang, J.; Yang, H.; Zeng, B.; Xiao, Y.; Liu, J. Optimization Method of Oriented Perforation Parameters Improving Uneven Fractures Initiation for Horizontal Well Fracturing. *Fuel* **2023**, *349*, 128754. [CrossRef]
9. Li, X.-S.; Wang, Y.; Zhang, Y. Optimization of the Production Pressure for Hydrate Dissociation by Depressurization. *Energy Fuels* **2020**, *34*, 4296–4306. [CrossRef]
10. Peng, G. Fracture Propagation Laws of Staged Hydraulic Fracture in Fractured Geothermal Reservoir Based on Phase Field Model. *Int. J. Coal Sci. Technol.* **2023**, *10*, 52. [CrossRef]
11. Bin, L.; Jingan, L.; Kaixiang, S.; Yanjiang, Y.; Bo, L. Thermo-Pressure Coupling Model for Gas Hydrate Depressurization Exploitation in South China Sea. *Energy Explor. Exploit.* **2024**, *42*, 2218–2240. [CrossRef]
12. Qi, R.; Lu, H.; Xu, C.; Yu, L.; Xiao, C.; Du, J.; Li, Y. Study on the Evolution Law of Temperature, Pressure, and Productivity near the Well for Gas Hydrate Exploitation by Depressurization. *Energies* **2024**, *17*, 3728. [CrossRef]
13. Wani, S.; Samala, R.; Kandasami, R.K.; Chaudhuri, A. Extraction-Induced Deformation in the Gas Hydrate Reservoir Using a Multiphase-Coupled THMC Solver. In Proceedings of the Geo-Congress 2024, Vancouver, BC, Canada, 25–28 February 2024; pp. 72–81. [CrossRef]
14. Kwon, T.H.; Cho, G.C.; Santamarina, J.C. Gas Hydrate Dissociation in Sediments: Pressure-Temperature Evolution. *Geochem. Geophys. Geosyst.* **2008**, *9*, Q03019. [CrossRef]
15. Fitzgerald, G.C.; Castaldi, M.J. Thermal Stimulation Based Methane Production from Hydrate Bearing Quartz Sediment. *Ind. Eng. Chem. Res.* **2013**, *52*, 6571–6581. [CrossRef]
16. Li, B.; Li, X.-S.; Li, G.; Feng, J.-C.; Wang, Y. Depressurization Induced Gas Production from Hydrate Deposits with Low Gas Saturation in a Pilot-Scale Hydrate Simulator. *Appl. Energy* **2014**, *129*, 274–286. [CrossRef]
17. Zhao, J.; Zhu, Z.; Song, Y.; Liu, W.; Zhang, Y.; Wang, D. Analyzing the Process of Gas Production for Natural Gas Hydrate Using Depressurization. *Appl. Energy* **2015**, *142*, 125–134. [CrossRef]
18. Qin, X.; Liang, Q.; Ye, J.; Yang, L.; Qiu, H.; Xie, W.; Liang, J.; Lu, J.; Lu, C.; Lu, H.; et al. The Response of Temperature and Pressure of Hydrate Reservoirs in the First Gas Hydrate Production Test in South China Sea. *Appl. Energy* **2020**, *278*, 115649. [CrossRef]
19. Misyura, S.Y.; Donskoy, I.G. Dissociation of Natural and Artificial Gas Hydrate. *Chem. Eng. Sci.* **2016**, *148*, 65–77. [CrossRef]
20. Huang, L.; Xu, C.; Xu, J.; Zhang, X.; Xia, F. The Depressurization of Natural Gas Hydrate in the Multi-Physics Coupling Simulation Based on a New Developed Constitutive Model. *J. Nat. Gas Sci. Eng.* **2021**, *95*, 103963. [CrossRef]
21. Li, D.; Ren, S.; Zhang, L.; Liu, Y. Dynamic Behavior of Hydrate Dissociation for Gas Production via Depressurization and Its Influencing Factors. *J. Pet. Sci. Eng.* **2016**, *146*, 552–560. [CrossRef]
22. Shagapov, V.S.; Chiglintseva, A.S.; Rusinov, A.A. Theoretical Modeling of Gas Extraction from a Partially Gas-Saturated Porous Gas-Hydrate Reservoir with Respect to Thermal Interactions with Surrounding Rocks. *Theor. Found. Chem. Eng.* **2016**, *50*, 449–458. [CrossRef]
23. Fang, Y.-X.; Survey, C.G.S.G.M.G.; Lu, J.-A.; Liang, J.-Q.; Kuang, Z.-G.; Cao, Y.-C.; Chen, D.-F. Numerical Studies of Gas Hydrate Evolution Time in Shenhu Area in the Northern South China Sea. *China Geol.* **2019**, *2*, 49–55. [CrossRef]

24. Su, M.; Yang, R.; Wang, H.; Sha, Z.; Liang, J.; Wu, N.; Qiao, S.; Cong, X. Gas Hydrates Distribution in the Shenhu Area, Northern South China Sea: Comparisons between the Eight Drilling Sites with Gashydrate Petroleum System. *Geol. Acta* **2016**, *14*, 79–100. [CrossRef]
25. Zhang, L.; Zhang, C.; Zhang, K.; Zhang, L.; Yao, J.; Sun, H.; Yang, Y. Pore-Scale Investigation of Methane Hydrate Dissociation Using the Lattice Boltzmann Method. *Water Resour. Res.* **2019**, *55*, 8422–8444. [CrossRef]
26. Hardwick, J.S.; Mathias, S.A. Masuda's Sandstone Core Hydrate Dissociation Experiment Revisited. *Chem. Eng. Sci.* **2018**, *175*, 98–109. [CrossRef]
27. Lenhard, R.J.; Parker, J.C.; Mishra, S. On the Correspondence between Brooks-Corey and van Genuchten Models. *J. Irrig. Drain. Eng.* **1989**, *115*, 744–751. [CrossRef]
28. Sun, X.; Nanchary, N.; Mohanty, K.K. 1-D Modeling of Hydrate Depressurization in Porous Media. *Transp. Porous Media* **2005**, *58*, 315–338. [CrossRef]
29. Sun, J.; Zhang, L.; Ning, F.; Lei, H.; Liu, T.; Hu, G.; Lu, H.; Lu, J.; Liu, C.; Jiang, G.; et al. Production Potential and Stability of Hydrate-Bearing Sediments at the Site GMGS3-W19 in the South China Sea: A Preliminary Feasibility Study. *Mar. Pet. Geol.* **2017**, *86*, 447–473. [CrossRef]
30. Gu, Y.; Sun, J.; Qin, F.; Ning, F.; Li, Y.; Cao, X.; Liu, T.; Wang, R.; Jiang, G. Numerical Analysis on Gas Production from Silty Hydrate Reservoirs in the South China Sea by Depressurizing: The Effect of Permeability Reduction Caused by Pore Compression. *J. Nat. Gas Sci. Eng.* **2022**, *104*, 104680. [CrossRef]
31. Cao, X.; Sun, J.; Qin, F.; Ning, F.; Mao, P.; Gu, Y.; Li, Y.; Zhang, H.; Yu, Y.; Wu, N. Numerical Analysis on Gas Production Performance by Using a Multilateral Well System at the First Offshore Hydrate Production Test Site in the Shenhu Area. *Energy* **2023**, *270*, 126690. [CrossRef]

Disclaimer/Publisher's Note: The statements, opinions and data contained in all publications are solely those of the individual author(s) and contributor(s) and not of MDPI and/or the editor(s). MDPI and/or the editor(s) disclaim responsibility for any injury to people or property resulting from any ideas, methods, instructions or products referred to in the content.